

Article

Research on a Super-Sub-Arc Bivariate Relative Angle Thermal Deformation Testing Method without Pitch Angle Limitation

Yang Liu ^{1,2}, Yaoke Xue ^{1,2,3,4}, Hu Wang ^{1,2,5,6,*}, Yue Pan ^{1,2}, Shangmin Lin ^{1,2}, Shuifu Ye ^{1,2} and Jie Liu ^{1,2}

- ¹ Xi'an Institute of Optics and Precision Mechanics, Chinese Academy of Sciences, Xi'an 710119, China; liuyang7203@opt.ac.cn (Y.L.); xueyaoke@opt.ac.cn (Y.X.); panyue@opt.ac.cn (Y.P.); linshangmin@opt.ac.cn (S.L.); cqfchen35@gmail.com (S.Y.); liujie0716@opt.ac.cn (J.L.)
- ² Xi'an Space Sensor Optical Technology Engineering Research Center, Xi'an 710119, China
- ³ Youth Innovation Promotion Association of Chinese Academy of Sciences, Beijing 100037, China
- ⁴ School of Instrumentation Science and Optoelectronic Engineering, Beihang University, Beijing 100191, China
- ⁵ University of Chinese Academy of Sciences, Beijing 100049, China
- ⁶ Laboratory of Sciences Space Precision Measurement Technology of Chinese Academy of Sciences, Xi'an 710119, China
- * Correspondence: wanghu@opt.ac.cn

Abstract: In light of the current situation where no testing equipment is available for measuring thermal deformation of objects, this paper proposes a novel method for accurate and precise measurement. The method overcomes the limitations of previous approaches that relied on pitch angle. By utilizing the principle of biplane multiple reflections, a bivariate laser spot displacement analysis algorithm is devised to attain highly precise measurements of bivariate angles. Additionally, a temperature gradient comparison algorithm is introduced to calculate the indicator test results under specific temperature conditions. To validate the effectiveness and reliability of this method, a testing system is constructed and utilized. The results demonstrate that the thermal deformation angle change test achieves an impressive accuracy of $0.015''$ and a rate of thermal deformation angle change of $0.3247''/^\circ\text{C}$. These values are in close agreement with the previously simulated analysis result of $0.359''/^\circ\text{C}$, with only a relative error of 9.55%. Therefore, the test results confirm the efficacy and reliability of this testing method along with the feasibility of the algorithm processing.



Citation: Liu, Y.; Xue, Y.; Wang, H.; Pan, Y.; Lin, S.; Ye, S.; Liu, J. Research on a Super-Sub-Arc Bivariate Relative Angle Thermal Deformation Testing Method without Pitch Angle Limitation. *Appl. Sci.* **2023**, *13*, 9725. <https://doi.org/10.3390/app13179725>

Academic Editor: Andrés Márquez

Received: 22 July 2023

Revised: 16 August 2023

Accepted: 25 August 2023

Published: 28 August 2023



Copyright: © 2023 by the authors. Licensee MDPI, Basel, Switzerland. This article is an open access article distributed under the terms and conditions of the Creative Commons Attribution (CC BY) license (<https://creativecommons.org/licenses/by/4.0/>).

Keywords: not limited by pitch angle; thermal deformation; bivariate angle; ultra-sub-arc; position-sensitive device; displacement coordinate analysis algorithm; matrix comparison method; integrated measurement equipment

1. Introduction

High-resolution microangle measurement techniques have rapidly evolved, playing a crucial role in various fields, particularly in aerospace [1]. In astronomical exploration, the thermal deformation of large-aperture spliced mirrors directly determines the imaging quality: for example, the James Webb Telescope (Figure 1), successfully launched in 2021, has a main mirror diameter of 6.5 m and is composed of 18 sub-mirrors spliced together [2,3]. Similarly, the effective aperture of the TMT (Figure 2) Third Realm under construction has reached 30 m, consisting of 492 hexagonal fragments [4]. The thermal deformation of these spliced mirrors due to temperature changes must be accurately determined. By using an independent sub-mirror support system and a common phase correction system (i.e., sub-mirror common phase correction device), the influence of temperature and other factors on the spatial position of the mirror can be corrected, achieving a sub-mirror confocal common phase [5–8] and achieving the optimal performance of large-aperture splicing mirrors.

Similarly, in the calibration of star sensors, the thermal deformation of the support frame of the dome-type multi-star simulator (Figure 3) significantly impacts the star map simulation accuracy of the simulator [9–12]. By identifying the thermal deformation

direction of the support frame, timely correction of the thermal deformation error can improve the simulation accuracy of the star simulator.

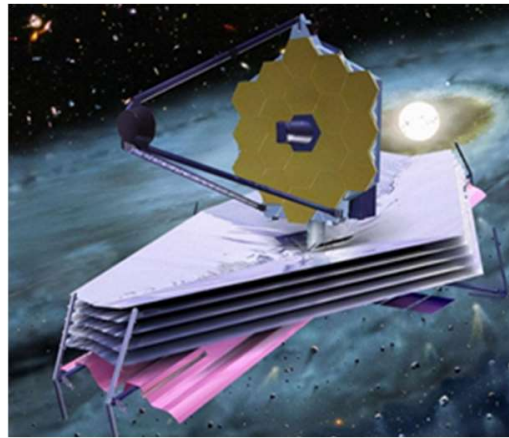


Figure 1. James Webb Space Telescope (JWST) [2].

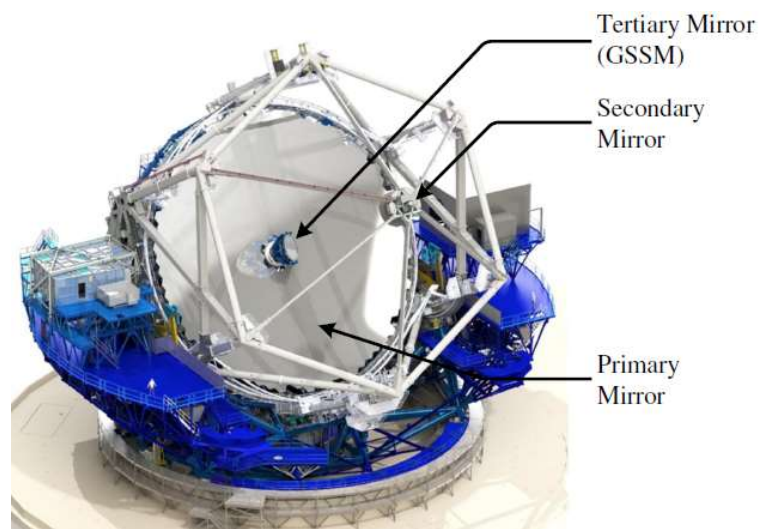


Figure 2. Thirty Meter Telescope (TMT) [4].

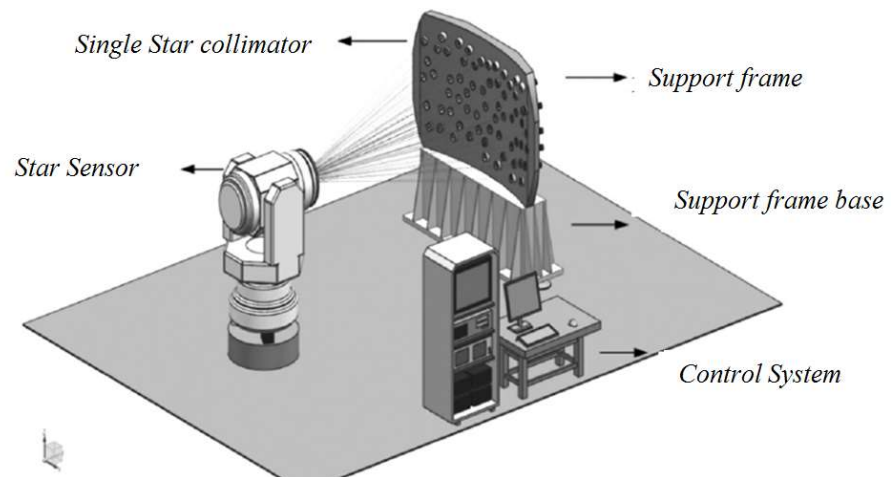


Figure 3. Schematic diagram of a large field of view multi star simulator [12].

However, the evaluation of thermal deformation currently relies primarily on simulation analysis and lacks direct testing of object deformation. Several unresolved issues contribute to this limitation:

Firstly, the thermal deformation of an object is generally elastic deformation, and the change in the normal direction angle of the test area is measured in arc, sub-arc, or even ultra-sub-arc, and it is tested at any elevation angle. Currently, the only testing equipment with a testing accuracy of $0.01''$ is the Muller HR photoelectric autocollimator [13]. However, this device's testing is limited to the horizontal direction within a 10° field of view to achieve the desired accuracy [14]. Therefore, this device cannot be used for thermal deformation testing. It can be seen that there is currently no equipment that can meet the requirements for the thermal deformation index such as the change in direction of the surface normal.

Secondly, conventional small-angle testing studies are conducted on univariate angle changes. The change in the normal direction of a single part of an object is a single variable of thermal deformation. The testing of this single variable cannot directly reflect the deformation of the object as it cannot remove the rigid displacement of the entire object. The change in the relative angle between the surface normals of different parts of the test object in space can directly reflect the deformation of the object by removing the overall rigid displacement change of the object. This requires testing the changes in the spatial relative angle between two variables, that is, testing the changes in the angle between two variables, which is a new problem.

Lastly, the thermal deformation index is proposed under specific temperature conditions. However, it is difficult to consistently replicate these exact temperature conditions during testing. Therefore, we cannot directly obtain indicator test results, which is also a problem that needs to be addressed.

This paper proposes a high-precision thermal deformation index testing scheme, which provides valuable insights for related thermal deformation index testing.

2. Testing Methods

2.1. Theoretical Basis of Ultra-Sub-Arc-Level Angle Measurement

For long-distance small-angle testing, we usually consider using optical non-contact measurement methods, such as the autocollimation method [15,16], Moire fringe method [17,18], internal reflection reflectance method [19], internal reflection interference phase method [20,21], etc.

The biplane reflection calculates the angle change value through the displacement change value of the light spot [22] as shown in Figure 4: two plane reflector mirrors are parallel to each other. One of them serves as the target plane mirror, rigidly fixed with the measured object, deflecting along with the measured object, while the other plane mirror serves as the reference reflector mirror. The laser and the spot position detector are separated on the left and right sides of the reference plane reflector mirror. The laser is incident at a small angle, forming n reflections between two biplane mirrors. The final output laser is received by the spot position detector, recording the initial position of the light spot. The distance between the light spot and the emitting end is:

$$S_0 = 2nH \tan \alpha \quad (1)$$

S_0 is the initial position of the laser spot, α is the incident angle of the laser, H is the distance between two planar mirrors, and n is the number of times the laser reflects between two plane reflector mirrors, as shown in Figure 4.

When the measured object is deflected along with the target plane reflector mirror $\Delta\theta$, the light spot on the detector will generate a displacement ΔS , with a total displacement of S :

$$S \approx H \tan \alpha + \sum_{i=1}^{n-1} 2H \tan(\alpha + 2i\Delta\theta) + H \tan(\alpha + 2n\Delta\theta) \quad (2)$$

Displacement of light spot ΔS can be approximated as:

$$\Delta S = S - S_0 \approx 2n^2 H \Delta\theta \quad (3)$$

$$\Delta\theta = \arctan\left(\frac{\Delta S}{2n^2H}\right) \approx \frac{\Delta S}{2n^2H} \tag{4}$$

$$d\theta \approx \frac{ds}{2n^2H} < 0.1'' \tag{5}$$

Among them, $d\theta$ represents the angle testing accuracy and ds represents the displacement resolution of the spot position detector.

We can see from Equation (5) that both increasing the number of reflection cycles n and increasing the distance H of the double-sided mirror can improve the sensitivity of angle measurement. As long as we select a detector with appropriate resolution and match the number of reflections n and the testing distance H , we can theoretically obtain a testing accuracy of ultra-sub-arc. Moreover, this testing principle is not limited by the pitch angle and can be tested at any pitch angle.

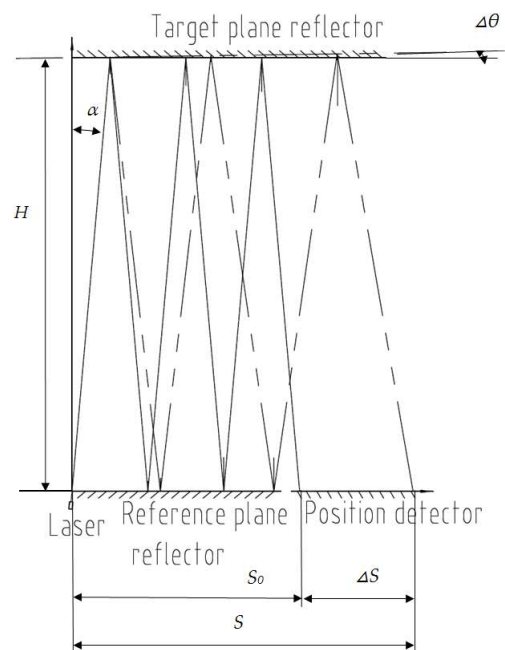


Figure 4. Measuring Principle.

2.2. Dual-Variable Angle Variation Test

We can see from Equation (4) that the angle change value is calculated through the displacement change value of the light spot. Therefore, we can also calculate the change value of the bivariate angle through the relative displacement value of the bivariate spot for testing.

To calculate the relative displacement of the bivariate laser spot, we first need to convert the displacement S_i measured at different reflection times n_i and testing distance H_i to the uniform displacement S_i' of the spot under the conditions of reflection times n and testing distance H . Then, through vector calculation, we obtain the relative displacement value ΔS of the bivariate laser spot. Finally, we calculate the relative angle change value of the two variables according to Equation (4).

We assume two variables: O_1 and O_2 ; the test parameters for variable O_1 are: reflection number n_1 and distance H_1 , spot displacement S_1 , and the test parameters for variable O_2 are: reflection number n_2 and distance H_2 , spot displacement S_2 .

Based on the test parameters of variable O_1 , we convert S_2 measured under $O_2, n_2,$ and H_2 conditions to S_2' under $O_1, n_1,$ and H_1 conditions:

$$\frac{S_2'}{S_2} = \frac{2n_1^2 H_1}{2n_2^2 H_2} \tag{6}$$

We can see from Equation (6) that the conversion of displacement only changes the numerical value and does not change the vector direction of O_2 displacement. The relative displacement ΔS of the dual laser spot is:

$$\Delta S = S_1 + S_2' \tag{7}$$

We then calculate the relative angle change value $\Delta\theta$ of the two variables based on Equation (4), and the schematic diagram of relative displacement calculation is shown in Figure 5.

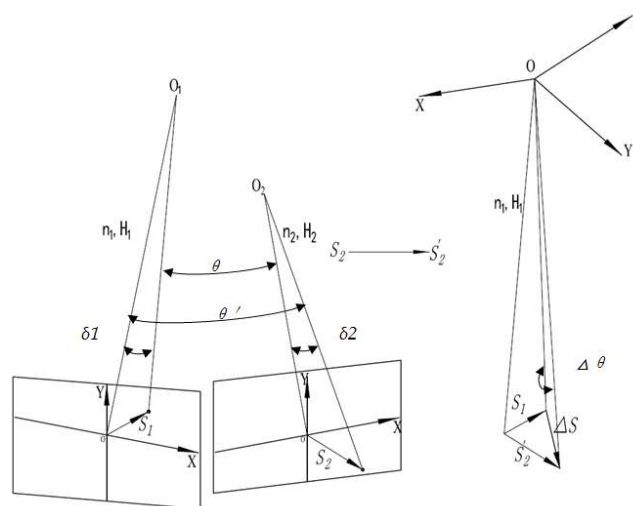


Figure 5. Schematic diagram of displacement conversion.

2.3. Conversion Algorithm for Thermal Conditions

We know that the thermal deformation of linear materials is directly proportional to temperature within the temperature range of the linear expansion coefficient. Therefore, we can infer that within the linear temperature range, the thermal deformation μ between the two temperature measuring points of the linear material is directly proportional to the magnitude of the temperature gradient (ΔT), as shown in Equation (8).

We use the discretization mathematical idea to set the temperature control conditions as the small grid temperature matrix, as shown in Figure 6.

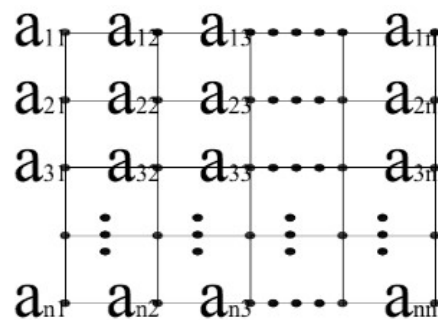


Figure 6. Temperature control temperature matrix.

We can further infer that the ratio of thermal deformation (μ') under the actual temperature gradient (ΔT_0) to the thermal deformation (μ_0) under the specified temperature gradient ($\Delta T'$) is directly proportional to the ratio of the two temperature gradients, as shown in Equation (9):

$$\mu = \sigma \Delta T \tag{8}$$

$$\frac{\mu_0}{\mu'} = \frac{\Delta T_0}{\Delta T'} \tag{9}$$

We use the discretization mathematical idea to set the temperature control conditions as the small grid temperature matrix, as shown in Figure 6. We obtain the set temperature gradient matrix (ΔT_{0-row}) by decomposing the set temperature conditions and calculate the actual temperature gradient matrix ($\Delta T_{row}'$) from the actual temperature matrix, for example, the row direction temperature gradient matrix as shown in Equation (10).

$$\Delta T_{0-row} = \begin{bmatrix} t_{11} & t_{12} & t_{13} & \dots\dots & t_{1,n-1} \\ t_{21} & t_{22} & t_{23} & \dots\dots & t_{2,n-1} \\ t'_{31} & t'_{32} & t'_{33} & \dots\dots & t'_{3,n-1} \\ \vdots & \vdots & \vdots & \vdots & \vdots \\ t_{m-1,1} & t_{m-1,2} & t_{m-1,3} & \dots\dots & t_{m-1,n-1} \end{bmatrix}$$

$$\Delta T_{row}' = \begin{bmatrix} t'_{11} & t'_{12} & t'_{13} & \dots\dots & t'_{1,n-1} \\ t'_{21} & t'_{22} & t'_{23} & \dots\dots & t'_{2,n-1} \\ t'_{31} & t'_{32} & t'_{33} & \dots\dots & t'_{3,n-1} \\ \vdots & \vdots & \vdots & \vdots & \vdots \\ t'_{m-1,1} & t'_{m-1,2} & t'_{m-1,3} & \dots\dots & t'_{m-1,n-1} \end{bmatrix} \tag{10}$$

We calculate the ratio of the corresponding elements of two matrices, as shown in Equation (11), and obtain a comparison matrix N , as shown in Equation (12). We use the concept of a mathematical matrix norm to calculate the norm formula of the comparison matrix N , as shown in Equation (13).

Setting:

$$n_{ij} = \frac{|t'_{ij}|}{|t_{ij}|} \tag{11}$$

That is:

$$N_{row} = \begin{bmatrix} n_{11} & n_{12} & n_{13} & \dots\dots & n_{1,n-1} \\ n_{21} & n_{22} & n_{23} & \dots\dots & n_{2,n-1} \\ n_{31} & n_{32} & n_{33} & \dots\dots & n_{3,n-1} \\ \vdots & \vdots & \vdots & \vdots & \vdots \\ n_{m,1} & n_{m,1} & n_{m,3} & \dots\dots & n_{m,n-1} \end{bmatrix} \tag{12}$$

$$N_{row} = \sum_{i=1}^m \sum_{j=1}^{n-1} \|n_{ij}\| \tag{13}$$

Similarly, the column direction comparison matrix norm is:

$$N_{col} = \sum_{j=1}^n \sum_{i=1}^{m-1} \|n_{ij}\| \quad (14)$$

Therefore, the average norm of the ratio matrix, which is the average multiplier of the temperature gradient, is:

$$N_{matrix \text{ mean norm}} = \frac{N_{row} + N_{col}}{E_{row-number \text{ elements}} + E_{col-number \text{ elements}}} \quad (15)$$

Among them, $E_{row-number \text{ elements}}$ represents the number of elements in the row direction magnification matrix. $E_{col-number \text{ elements}}$ represents the number of elements in the column direction magnification matrix.

According to the linear expansion law of materials, for example, Equation (9), the thermal deformation index under the set temperature gradient is:

$$\frac{\Delta\theta_0}{\Delta\theta'} = \frac{\Delta T_0}{\Delta T'} = N_{matrix \text{ mean norm}}$$

That is to say:

$$\Delta\theta_0 = \frac{\Delta\theta'}{N_{matrix \text{ mean norm}}} \quad (16)$$

3. Test and Verification

3.1. Test System Parameter Design

3.1.1. Introduction to Test Objectives

In order to verify the rationality of the above testing plan, we test the thermal stability of the support frame of a certain dome multi-star simulator. The schematic diagram of the support frame is shown in Figure 7, and the temperature gradient conditions of its thermal index is shown in Figure 8. Through finite element simulation analysis, we have learned that the thermal deformation rate of the angle between the installation surface normals of the two single-star parallel light tubes in the upper left and upper right corners of the support frame is $\nu = 0.359''/\text{°C}$, as shown in Figure 9. The physical definition of the rate of angular thermal deformation change is shown in Equation (17).

$$\nu = \frac{\Delta\theta}{\Delta T} \quad (17)$$

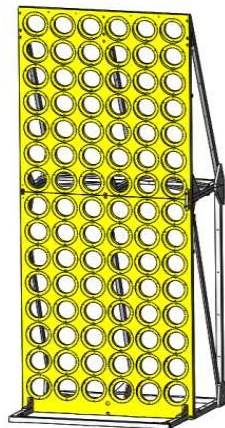


Figure 7. Schematic diagram of Support Frame.

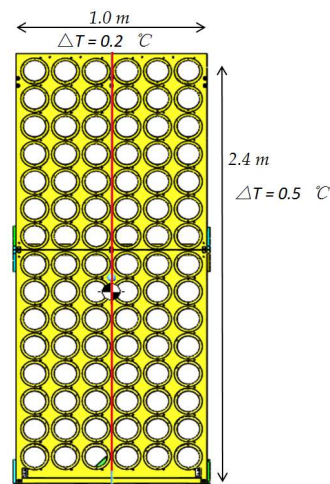


Figure 8. Schematic diagram of temperature conditions.

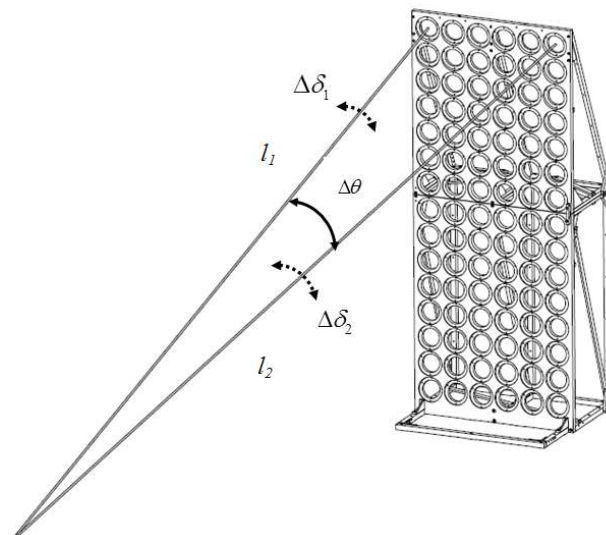


Figure 9. Schematic diagram of changes in thermal deformation angle.

Based on the testing plan, it can be seen that the rate of change in the angle at a specific temperature is:

$$v' = \frac{\Delta\theta_0}{\Delta T} = \frac{\Delta\theta'}{N_{matrix\ mean\ norm} * \Delta T} \tag{18}$$

At the same time, we can see from Figure 9 the left and right mirror symmetrical structure of the support frame, and the relative angle between the two normals is 6.71°, which means that the thermal deformation changes in its upper left and upper right mounting surfaces should be mirror symmetrical. Therefore, we only need to measure the change in normal direction of one of the single variables to simultaneously obtain the change in normal direction of the two variables.

3.1.2. Test System Parameter Design

According to the aforementioned testing methods, we have developed a dual-variable relative angle thermal deformation angle measurement system, which includes a laser spot detection unit, a biplane reflector unit, a post-processing unit, and a condition guarantee unit, the specific composition of which is shown in Figure 10. Among them, the biplane reflection unit and the laser spot detection unit are used for detecting deformation laser spot displacement changes, and the thermal control unit is used for the heating operation of the support frame.

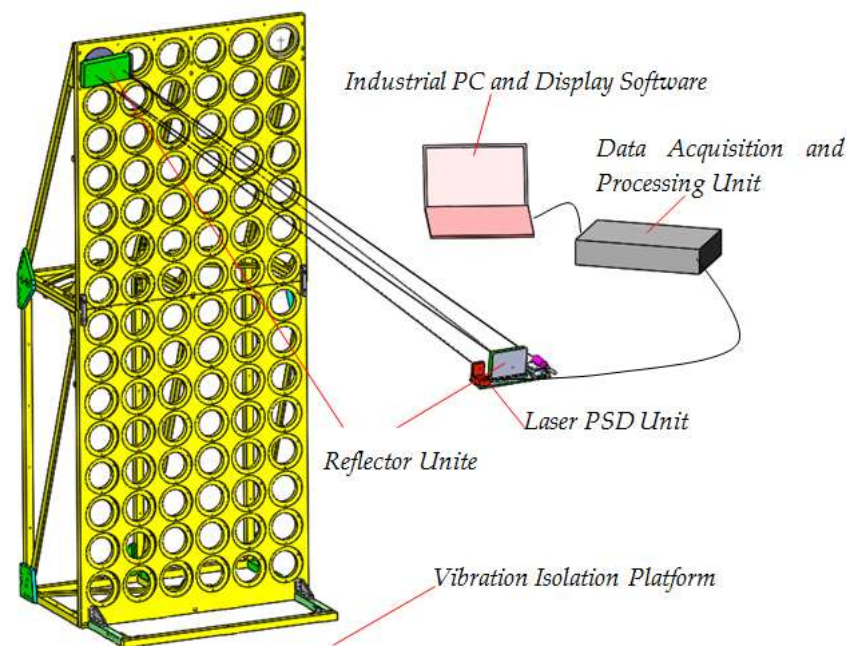


Figure 10. Layout diagram of testing system.

For laser spot displacement detectors, we choose position sensitive detector (PSD) devices [23]. This is because PSDs have the following advantages [24]: (1) the shape of the light spot does not affect the measurement of the displacement change value of the light spot by the PSD; (2) the PSD target resolution is extremely high and has achieved $1\ \mu\text{m}$ resolution; (3) the PSD has a high sampling frequency, which can output the spot coordinate value in real time, which is conducive to the development of test automation equipment in the later stage.

Therefore, PSDs are widely used in non-contact rapid measurement of displacement and distance [25]. Meanwhile, with the further evolution and optimization of PSDs, the measurement accuracy of PSDs will become more precise. For example, the 3CSiC/Si hetero structure proposed by Abu Riduan, Md Foisal et al. may be a position-sensitive detector [26], which is a promising choice in harsh environments (such as highly corrosive environments). Therefore, choosing PSDs in this study is more conducive to the later promotion and application of the testing plan. Therefore, choosing PSD devices is more conducive to the promotion and application of this scheme.

Finally, we select Shanghai Ou-guang Company's S2-0003-2L10-SU24 two-dimensional PSD and its controller [27]. Its resolution is $1\ \mu\text{m}$, effective photosensitive surface is $10 \times 10\ \text{mm}$, spectral response range is 380~1000 nm.

The composition of the entire testing system is shown in Figure 11. The laser passes through two reflection cycles and lands on the PSD, with two planar mirrors spaced at a distance of H of 3435 mm. According to the biplane reflection principle mentioned earlier, the parameters of the above testing system are brought into Equation (16), and the testing resolution of the testing system is $0.015''$, which can achieve angle testing accuracy of bivariate angles in super-sub-arc.

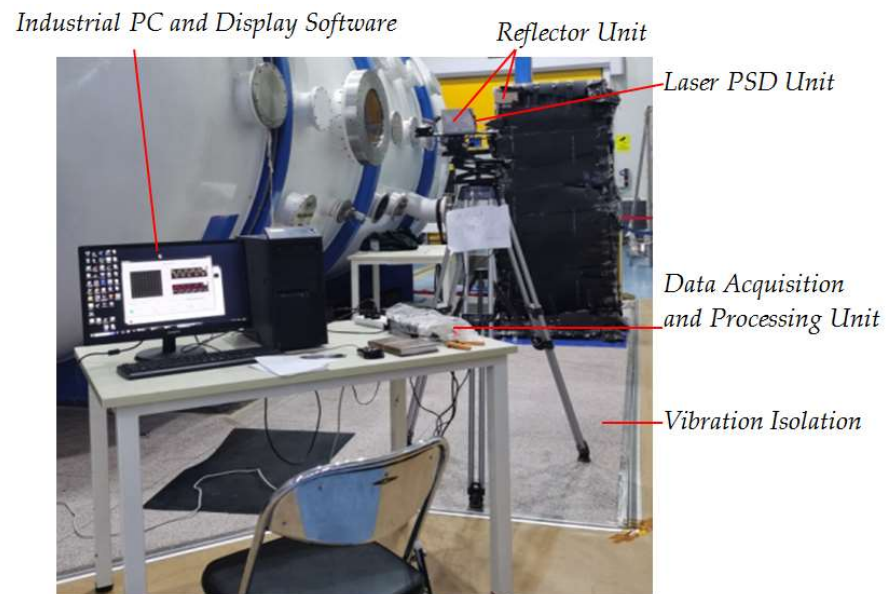


Figure 11. Principle sketch for the experiment.

Due to the thickness of the bottom plate of the support frame reaching 32 mm, under the condition of slow thermal conductivity of the frame material, there may be inconsistencies in the temperature values of the front and rear surfaces at the same position. For this purpose, heating plates and temperature measurement points are set on the front and back of the support frame bottom plate, and each is independently controlled for temperature. The coverage and thermal coating of the heating element implemented by the thermal control of the support frame are shown in Figure 12, and the distribution of the thermistor is shown in Figure 13. The temperature measurement accuracy of the thermistor used is ± 0.1 °C, and the appearance is shown in Figure 14.

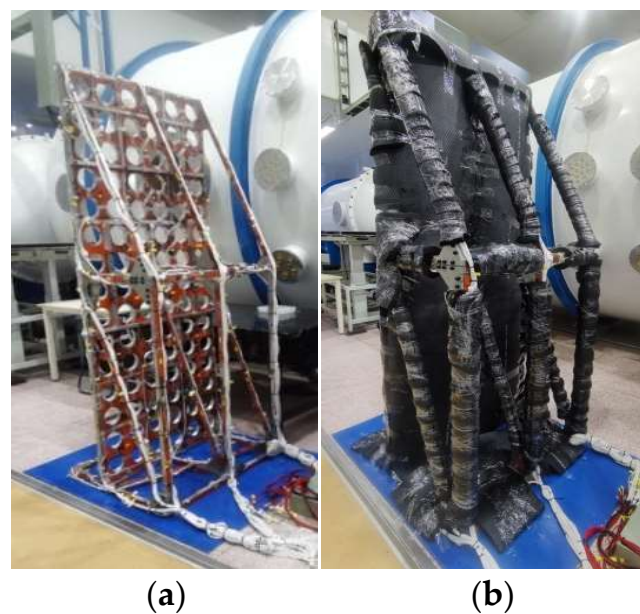


Figure 12. Thermal control implementation; (a) Pasting heating pads; (b) Thermal coating.

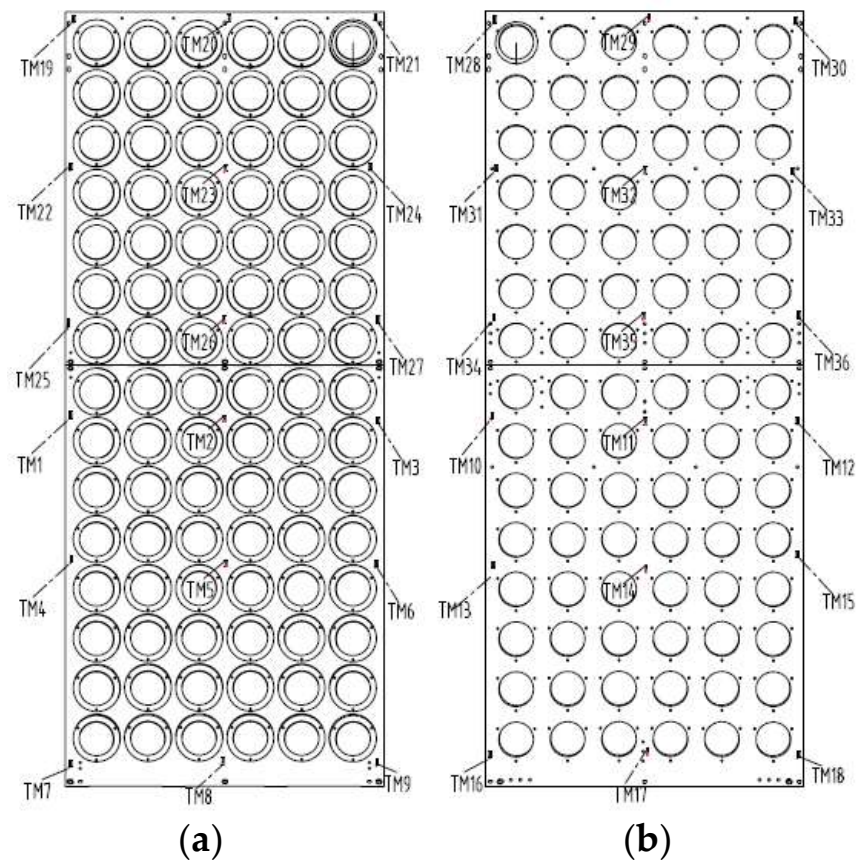


Figure 13. Distribution diagram of thermistor. (a) Front; (b) Back.

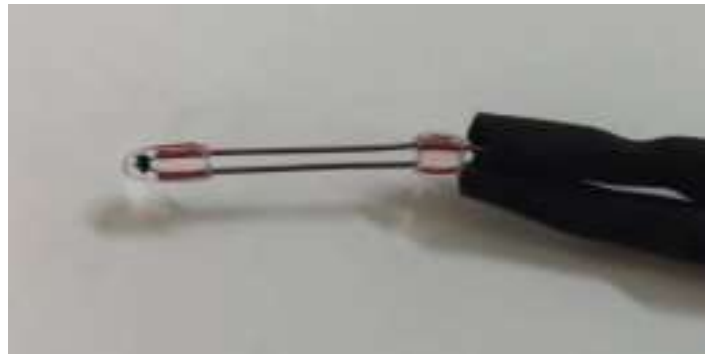


Figure 14. Thermistor sensor.

The target reflector is connected to the support frame through an adapter plate and leads out in the normal direction of the installation surface of the support frame, as is shown in Figure 15a. In order to avoid measurement errors caused by mirror deformation, we have taken the following two measures: (1) using an adapter plate made of invar 4J32 low thermal expansion coefficient material (thermal expansion coefficient $1.0 \times 10^{-6}/^{\circ}\text{C}$) to eliminate measurement errors caused by changes in mirror position caused by thermal deformation of the adapter plate; (2) the reflector and adapter plate are exposed without thermal coating to maintain consistency with the temperature in the laboratory hall, ensuring that the reflector itself does not undergo thermal deformation, as is shown in Figure 15b. By taking the above two measures, we eliminate the measurement error caused by the reflector.

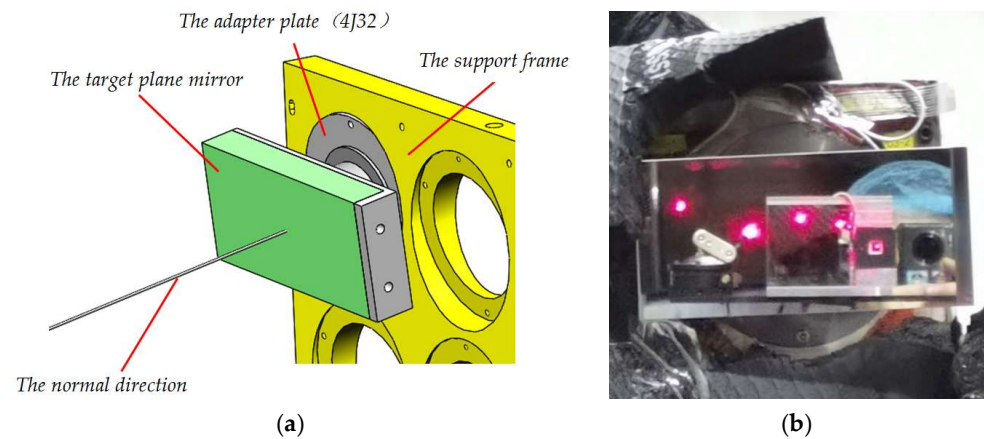


Figure 15. Installation diagram of target reflector; (a) Schematic diagram of target reflector connection; (b) The target reflector is exposed to the air.

3.1.3. Test Implementation

After setting up the testing system, we begin to experiment: the laser falls on the PSD target surface after two reflection cycles, as shown in Figure 16. We read the initial temperature matrix value of the support frame, as shown in Figure 17. The laser spot of the PSD is set to zero as shown in Figure 18, while reading the displacement drift error of the spot, as shown in Table 1. After the support frame is heated up by about 10 degrees Celsius, it is first kept warm for 1 h. The temperature matrix value after the heating is read for the second time, and after waiting for half an hour, the final temperature matrix value is read for the third time, as shown in Figure 19. The three temperature change curves are obtained, as shown in Figure 20. The PSD spot deviates, and the displacement deviation is shown in Figure 21. The displacement sampling values are shown in Figure 22.

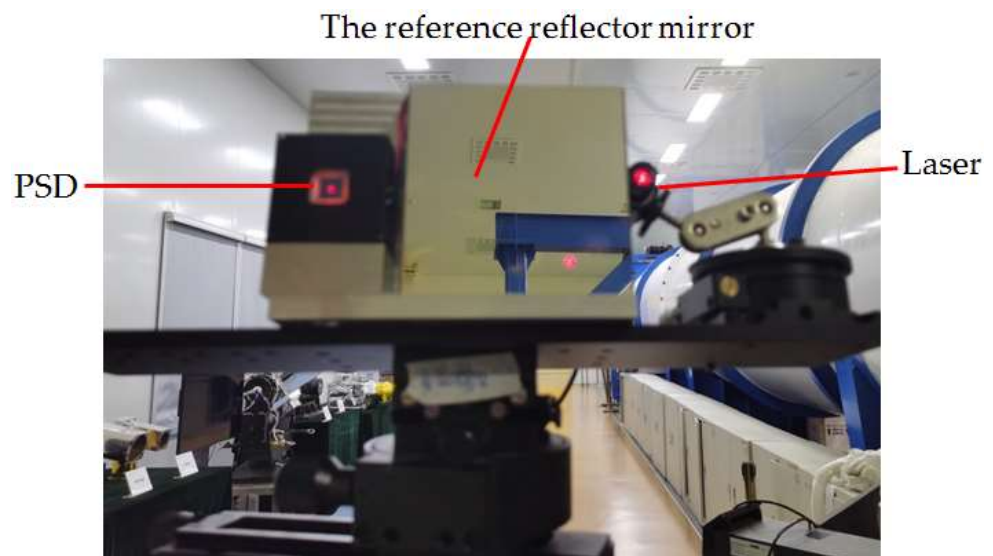


Figure 16. Laser reflection situation.

$$T_{front} = \begin{bmatrix} 26.6 & 26.1 & 26.8 \\ 27.0 & 26.9 & 26.1 \\ 26.4 & 26.9 & 26.7 \\ 26.5 & 26.1 & 27.2 \\ 26.9 & 25.9 & 26.3 \\ 28.2 & 27.7 & 26.9 \end{bmatrix}, \quad T_{back} = \begin{bmatrix} 26.4 & 27.2 & 26.1 \\ 26.7 & 26.7 & 26.3 \\ 26.3 & 26.7 & 26.2 \\ 26.4 & 27.0 & 26.5 \\ 26.2 & 27.6 & 26.1 \\ 27.7 & 26.5 & 27.3 \end{bmatrix}$$

Figure 17. Initial temperature matrix.

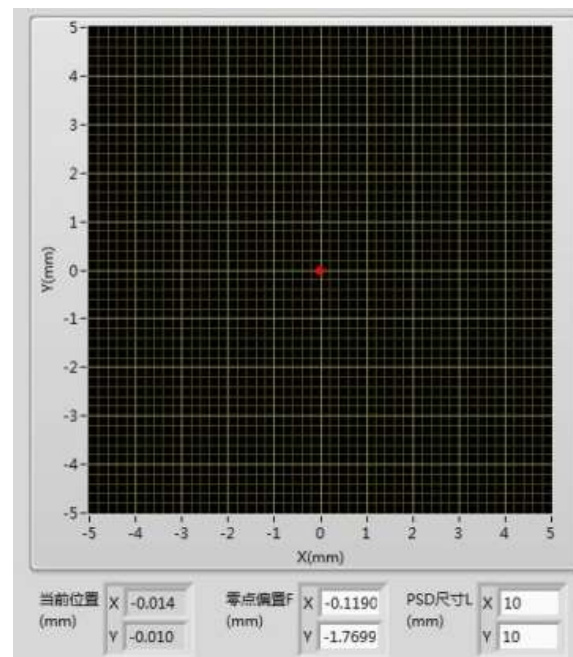


Figure 18. Schematic diagram of PSD displacement drift.

Table 1. PSD Spot Coordinate Zeroing Sampling.

Sampling	X	Y
1	-0.014	-0.01
2	0	-0.004
3	-0.003	-0.019
4	0.017	0.024
5	-0.003	-0.004
6	0.012	-0.047
7	0.005	-0.04
8	0.008	-0.007
9	0.012	0.014
Average drift error	0.003778	-0.01033

$$T'_{front} = \begin{bmatrix} 31.46 & 30.17 & 32.32 \\ 30.72 & 31.53 & 30.06 \\ 30.72 & 30.06 & 30.21 \\ 30.39 & 30.28 & 30.85 \\ 31.93 & 30.21 & 30.08 \\ 31.36 & 30.45 & 31.25 \end{bmatrix}, T'_{back} = \begin{bmatrix} 29.97 & 30.87 & 30.06 \\ 30.48 & 30.21 & 30.22 \\ 30.23 & 30.23 & 30.28 \\ 30.17 & 30.05 & 29.99 \\ 30.14 & 30.74 & 30.23 \\ 30.06 & 30 & 30.09 \end{bmatrix}$$

Figure 19. Final temperature matrix.

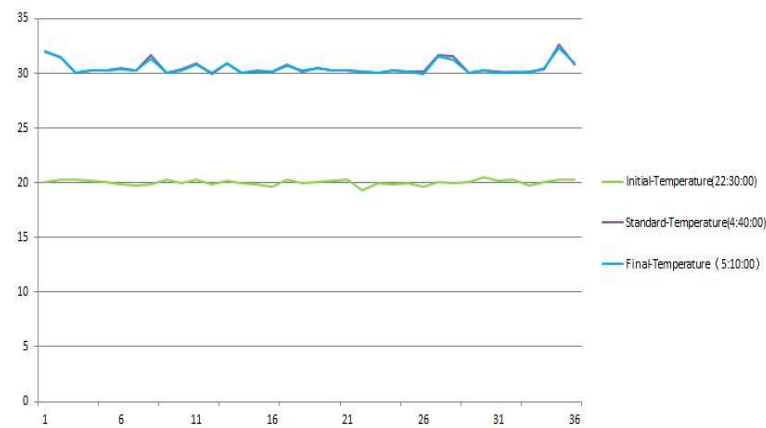


Figure 20. Temperature sampling curve for installing the base plate.

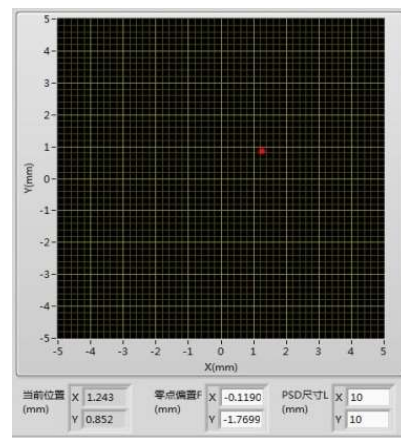


Figure 21. Laser spot displacement sampling for PSD devices.

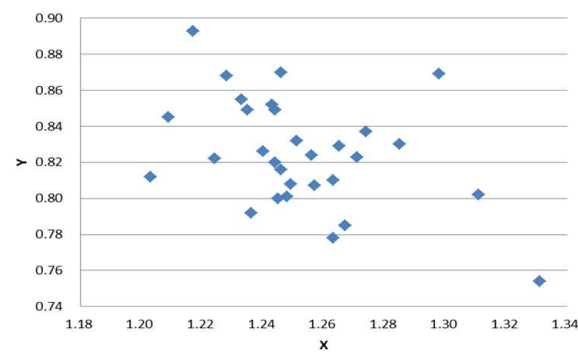


Figure 22. Spot displacement sampling point chart.

3.2. Calculation of Test Results

3.2.1. Calculation of Angle Test Results

Based on the collected experimental data, we first calculate the average displacement value of the laser spot and the average heating value of the support frame, as shown in Table 2. Then, using the symmetry of the support frame mirror image, we calculate the relative displacement value of the bivariate laser spot. The displacement vector calculation diagram is shown in Figure 23, and the displacement calculation is shown in Equation (19).

$$\left\{ \begin{array}{l} x_{1,vertical} = x_1 \cos \beta, \\ x'_1 = x_{1,vertical} \\ x'_2 = -x'_1 \\ x_1 = 1.24622, \beta = 3.355^\circ \\ \Delta S = \sqrt{(x'_1 - x'_2)^2} \end{array} \right. \quad (19)$$

Table 2. Calculation of spot displacement and temperature rise.

Displacement Direction	X ₁	Y ₁
Average displacement value (mm)	1.25	0.83
Average drift error (mm)	0.003778	−0.01033
Absolute displacement value (mm)	1.24622	0.8403
Average temperature change value ΔT (°C)	10.4633	

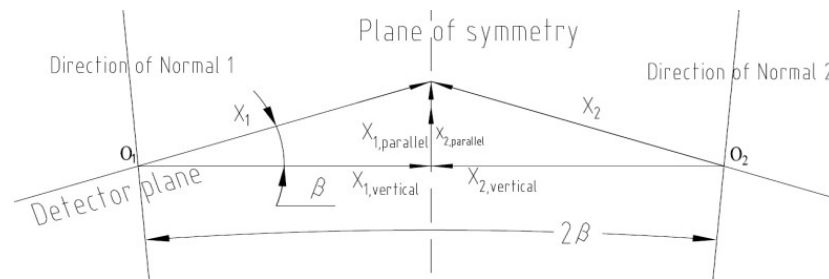


Figure 23. Coordinate System Conversion.

We insert the test parameters $H = 3435$ mm, $n = 2$, and ΔS into Equation (4) and obtain the relative angle change value of the two variables as:

$$\Delta\theta = 18.676''$$

3.2.2. Calculation of Thermal Condition Magnification

The temperature gradient required by the indicator is 0.2 °C in the row direction and 0.5 °C in the column direction. According to the uniform distribution of the actual temperature in the 6×3 matrix columns, the temperature gradient matrix in the row direction is a matrix of 6×2 , as shown in Equation (20). The temperature gradient matrix in the column direction is a matrix of 5×6 , as shown in Equation (21).

$$\Delta T_{row} = \begin{bmatrix} a_{11} & a_{12} \\ a_{21} & a_{22} \\ \vdots & \vdots \\ a_{12,1} & a_{12,2} \end{bmatrix} = \begin{bmatrix} 0.1 & 0.1 \\ 0.1 & 0.1 \\ \vdots & \vdots \\ 0.1 & 0.1 \end{bmatrix} \quad (20)$$

$$\Delta T_{col} = \left[\begin{array}{ccc|ccc} 0.1 & 0.1 & 0.1 & 0.1 & 0.1 & 0.1 \\ 0.1 & 0.1 & 0.1 & 0.1 & 0.1 & 0.1 \\ 0.1 & 0.1 & 0.1 & 0.1 & 0.1 & 0.1 \\ 0.1 & 0.1 & 0.1 & 0.1 & 0.1 & 0.1 \\ 0.1 & 0.1 & 0.1 & 0.1 & 0.1 & 0.1 \end{array} \right] \tag{21}$$

To calculate the temperature gradient comparison matrix in the row direction, we merge the two temperature matrices in Figure 19 into a temperature matrix with 12 rows and 3 columns:

$$T'_{row} = \left[\begin{array}{c} T'_{front} \\ T'_{back} \end{array} \right] = \left[\begin{array}{ccc} 31.46 & 30.17 & 32.32 \\ 30.72 & 31.53 & 30.06 \\ 30.72 & 30.06 & 30.21 \\ 30.39 & 30.28 & 30.85 \\ 31.93 & 30.21 & 30.08 \\ 31.36 & 30.45 & 31.25 \\ \hline 29.97 & 30.87 & 30.06 \\ 30.48 & 30.21 & 30.22 \\ 30.23 & 30.23 & 30.28 \\ 30.17 & 30.05 & 29.99 \\ 30.14 & 30.74 & 30.23 \\ 30.06 & 30 & 30.09 \end{array} \right]$$

We calculate the temperature gradient matrix $\Delta T'_{col}$ in the row direction:

$$\Delta T'_{row} = \left[\begin{array}{c} \Delta T'_{row,front} \\ \Delta T'_{row,back} \end{array} \right] = \left[\begin{array}{cc} 1.29 & 2.15 \\ 0.81 & 1.47 \\ 0.21 & 0.15 \\ 0.11 & 0.57 \\ 1.72 & 0.13 \\ \hline 0.91 & 0.8 \\ 0.9 & 0.81 \\ 0.27 & 0.01 \\ 0 & 0.05 \\ 0.12 & 0.06 \\ 0.6 & 0.51 \\ 0.06 & 0.09 \end{array} \right]$$

Similarly, in order to obtain the temperature gradient comparison matrix in the column direction, the two temperature matrices in Figure 16 are merged into a temperature matrix of 6 rows and 6 columns:

$$T'_{col} = \left[\begin{array}{c} T'_{front} \\ T'_{back} \end{array} \right] = \left[\begin{array}{ccc|ccc} 31.46 & 30.17 & 32.32 & 29.97 & 30.87 & 30.06 \\ 30.72 & 31.53 & 30.06 & 30.48 & 30.21 & 30.22 \\ 30.72 & 30.06 & 30.21 & 30.23 & 30.23 & 30.28 \\ 30.39 & 30.28 & 30.85 & 30.17 & 30.05 & 29.99 \\ 31.93 & 30.21 & 30.08 & 30.14 & 30.74 & 30.23 \\ 31.36 & 30.45 & 31.25 & 30.06 & 30 & 30.09 \end{array} \right]$$

We calculate the temperature gradient matrix $\Delta T'_{col}$ in the column direction:

$$\Delta T'_{col} = \left[\begin{array}{c} \Delta T'_{col,front} \\ \Delta T'_{col,back} \end{array} \right] = \left[\begin{array}{ccc|ccc} 0.74 & 1.36 & 2.26 & 0.51 & 0.66 & 0.16 \\ 0.45 & 1.47 & 0.15 & 0.25 & 0.02 & 0.06 \\ 0.12 & 0.22 & 0.64 & 0.06 & 0.18 & 0.29 \\ 1.54 & 0.07 & 0.77 & 0.03 & 0.69 & 0.24 \\ \hline 0.57 & 0.24 & 1.17 & 0.08 & 0.74 & 0.14 \end{array} \right]$$

By introducing Equations (11) and (12), the multiplication matrices for row and column directions are obtained as follows:

$$N_{row} = \begin{bmatrix} 12.9 & 21.5 \\ 8.1 & 14.7 \\ 2.1 & 1.5 \\ 9 & 8.1 \\ 2.7 & 0.1 \\ 0 & 0.5 \\ \hline 1.1 & 5.7 \\ 17.2 & 1.3 \\ 9.1 & 8 \\ 1.2 & 0.6 \\ 6 & 5.1 \\ 0.6 & 0.9 \end{bmatrix} \tag{22}$$

$$N_{col} = \begin{bmatrix} 7.4 & 13.6 & 22.6 & 5.1 & 6.6 & 1.6 \\ 4.5 & 14.7 & 1.5 & 2.5 & 0.2 & 0.6 \\ 1.2 & 2.2 & 6.4 & 0.6 & 1.8 & 2.9 \\ 15.4 & 0.7 & 7.7 & 0.3 & 6.9 & 2.4 \\ 5.7 & 2.4 & 11.7 & 0.8 & 7.4 & 1.4 \end{bmatrix} \tag{23}$$

By introducing Equations (13) and (14), the ratio matrix norm of the row direction and column direction is:

$$N_{row-number} = \sum_{i=1}^m \sum_{j=1}^{n-1} \|n_{ij}\| = 138; n_{row-number} = 12 * 2 = 24;$$

$$N_{col-number} = \sum_{j=1}^n \sum_{i=1}^{m-1} \|n_{ij}\| = 158.8; n_{col-number} = 5 * 6 = 30; \tag{24}$$

By introducing Equation (15), the average norm of the temperature gradient matrix is obtained as:

$$N_{mean} = N_{mean-norm} = \frac{N_{row-norm} + N_{col-norm}}{n_{row-number} + n_{col-number}} = 5.4963$$

3.2.3. Calculation of Test Results for Indicators

We substitute the results of the angle change of the relative angle between the two variables tested and the temperature condition multiplier value into Equation (16) and obtain the change value of the angle between the normal direction of the double-hole installation surface under the specific temperature gradient condition of the indicator as follows:

$$\Delta\theta_0 = \frac{\Delta\theta'}{N_{matrix\ mean\ norm}} = 3.398''$$

By introducing Equation (18), the final target test value is:

$$v' = \frac{\Delta\theta_0}{\Delta T} = \frac{\Delta\theta'}{N_{matrix\ mean\ norm} * \Delta T} = 0.3247'' / ^\circ C \tag{25}$$

3.3. Test Error Analysis

According to Equation (18), there are three sources of error in indicator testing: (1) angle testing error, $\varepsilon(\Delta\theta) = 0.015''$; (2) the temperature sensor thermistor temperature test error limit is $\varepsilon(\Delta T) = 0.2\ ^\circ C$, (3) the calculation error of temperature gradient

ratio N : $\varepsilon(\Delta N) = 0.2\text{ }^\circ\text{C}/0.1\text{ }^\circ\text{C} = 2$. The error in the rate of angle change under specified temperature conditions is:

$$\begin{aligned}\varepsilon(\Delta v_{set}) &= \left| \frac{\partial f}{\partial \Delta \theta} \right| \varepsilon(\Delta \theta) + \left| \frac{\partial f}{\partial \Delta T} \right| \varepsilon(\Delta T) + \left| \frac{\partial f}{\partial N} \right| \varepsilon(N) \\ \varepsilon(\Delta v_{set}) &= 0.126'' / ^\circ\text{C}\end{aligned}\quad (26)$$

The results of this testing system's indicators are:

$$v_{set} = 0.3247'' / ^\circ\text{C} \pm 0.126'' / ^\circ\text{C} \quad (27)$$

The relative error between the test results and the thermal deformation simulation analysis is:

$$\varepsilon_r = \frac{\|v' - v_0\|}{\|v_0\|} = 9.55\% \quad (28)$$

It can be seen that the relative error between the indicator test results and the thermal deformation simulation analysis results is 9.55%. The two are basically consistent.

4. Conclusions

This paper proposes a novel approach for thermal deformation testing, specifically focusing on the measurement of dual-variable angles. Building upon the current research on thermal deformation index testing, a measurement system has been developed and applied to the thermal deformation testing of a single star light tube support frame in a dome multi-star simulator. With a testing accuracy of $0.015''$, this system allows for super-sub-arc testing accuracy of dual-variable angles, even at different pitch angles. Through calculation, the relative deviation between the final test results of the support frame indicators and the simulation analysis results is 9.55%. The test results validate the correctness, reasonability, and feasibility of the proposed measurement scheme.

From the test error analysis results, it can be seen that the test verification scheme achieves a super sub angular second test accuracy of unrestricted pitch angle and relative deformation of different parts of the object. This paper transforms the conventional untested deformation indicators into testable indicators through technological innovation. This technology can be applied to the field of precise deformation testing, such as the deformation testing of sub mirrors of ground-based ultra large aperture reflection telescopes. The pose parameters of each sub mirror can be adjusted in real-time, or the relative deformation testing of ultra large aperture antennas can be carried out. Through the precision testing results of object relative deformation, we can timely correct the pose parameters of the equipment, ensuring that the equipment can have good working conditions and high indicator performance.

Author Contributions: Conceptualization, Y.L.; methodology, Y.L.; software, S.L.; validation, Y.X.; investigation, H.W.; resources, S.Y.; data curation, J.L.; writing—original draft preparation, Y.L.; writing—review and editing, Y.P. All authors have read and agreed to the published version of the manuscript.

Funding: This research was funded by the National Natural Science Foundation of China Grant No. 11803075.

Institutional Review Board Statement: Not applicable.

Informed Consent Statement: Not applicable.

Data Availability Statement: Not applicable.

Acknowledgments: The authors thank the outstanding work of the space sensor optical technology teams from Xi'an Institute of Optics and Precision Mechanics of the Chinese Academy of Sciences.

Conflicts of Interest: The authors declare no conflict of interest.

References

1. Li, J.-Y.; Wu, J.-T.; Han, H.-Q. Small angle measurement with optical methods and its application. *Appl. Sci. Technol.* **2006**, *33*, 15–16.
2. Hou, Y.-L.; Yang, F.; Wang, F.-G. Overview of key technologies for segmented mirrors of large-aperture optical telescopes. *Chin. Opt.* **2022**, *15*, 973–982.
3. Sahai, R. Observing Planetary and Pre-Planetary Nebulae with the James Webb Space Telescope. *Galaxies* **2020**, *8*, 61. [CrossRef]
4. Guo, P.; Zhang, J.; Yang, F.; Hu, H.; Jiang, H. Geometric layout optimization of a large aperture thin elliptical mirror's axial and lateral support. *Appl. Opt.* **2021**, *60*, 2861–2869. [CrossRef]
5. Shen, S.-D.; Cui, X.-Q.; Zhang, Y. Simulation and analysis of co-phasing errors of the segmented primary mirror tiled by hexagonal segments in LOT. *Res. Astron. Astrophys.* **2021**, *21*, 245. [CrossRef]
6. Hu, J.-N.; Dong, J.-H.; Zhou, P.-W. Review on active support system of large ground-based telescope primary mirror. *Laser Infrared* **2017**, *47*, 5–12.
7. Xu, H.; Yang, L.-W.; Yang, H.-S. Recent progress of active support system for large optical telescope primary mirror. *Laser Optoelectron. Prog.* **2018**, *55*, 11–23.
8. Li, X.P.; Shi, J.F.; Wang, W.; Wang, Y.J.; Fan, X.W. Review on splicing structure technology of large aperture space primary mirror. *Laser Optoelectron. Prog.* **2018**, *55*, 22–34.
9. Liu, M.; Wang, H.; Yi, H.; Xue, Y.; Wen, D.; Wang, F.; Shen, Y.; Pan, Y. Space Debris Detection and Positioning Technology Based on Multiple Star Trackers. *Appl. Sci.* **2022**, *12*, 3593. [CrossRef]
10. Liu, M.; Wei, X.; Wen, D.; Wang, H. Star Identification Based on Multilayer Voting Algorithm for Star Sensors. *Sensors* **2021**, *21*, 3084. [CrossRef]
11. Xu, H.-G.; Han, B.; Li, M.L.; Ma, H.T.; Zhang, P.Y.; Ju, D.H. Design and verification of high-precision multi-star simulator with a wide field of view. *Chin. Opt.* **2020**, *13*, 1343–1351.
12. Li, M.L.; Han, B.; Liu, H.; Yuan, L.; Huang, D.F. Study on Calibration Technology of Large Field of View Multi-star Simulator. *J. Changchun Univ. Sci. Technol. (Nat. Sci. Ed.)* **2020**, *43*, 17–22.
13. Huang, Y.-G. Study on Micro-Angle Measuring Basic Technique of Laser Autocollimation. Ph.D. Thesis, Tianjin University, Tianjin, China, 2009.
14. ELCOMAT HR Operation Manual. MÖLLER-WEDEL OPTICAL: Wedel, Germany. Available online: <https://www.haag-streit.com/moeller-wedel-optical/products/electronic-autocollimators/elcomat-product-line/elcomat-hr/> (accessed on 24 August 2023).
15. Konyakhin, I.A.; Timofeev, A.N.; Konyakhin, A. Three-axis optic-electronic autocollimation system for the inspection of large-scale objects. In Proceedings of the SPIE Optical Metrology 2013, Munich, Germany, 13–16 May 2013; Volume 8788, p. 87882C-1-8.
16. Konyakhin, I.A.; Kopylova, T.V.; Konyakhin, A.I. Optic-electronic autocollimation sensor for measurement of the three-axis angular deformation of industry objects. In Proceedings of the SPIE Photonics Europe, Brussels, Belgium, 16–19 April 2012; Volume 8439, p. 84391N-1-7.
17. Di, C.; Yan, W.; Hu, S.; Yin, D.; Ma, C. Moire-Based absolute interferometry with large measurement range in Wafer-Mask alignment. *IEEE Photonics Technol. Lett.* **2015**, *27*, 435–438. [CrossRef]
18. Wang, Q.-H.; Ri, S.; Tsuda, H. Digital sampling Moireas asubstitute for microscope scanning Moire for high-sensitivity and full-field deformation measurement at micron/nano scales. *Appl. Opt.* **2016**, *55*, 6858–6885. [CrossRef] [PubMed]
19. Zhang, A.-Y.; Huang, P.-S. Total internal reflection for precision small-angle measurement. *Appl. Opt.* **2001**, *40*, 167–1622. [CrossRef] [PubMed]
20. Chui, M.-H.; Wang, S.-F.; Chang, R.-S. Instrument for measuring small angles by use of multiple total internal reflection in heterodyne interferometry. *Appl. Opt.* **2004**, *43*, 5438–5442. [CrossRef]
21. Lin, J.-Y.; Liao, Y.-C. Small-angle measurement with highly sensitive total internal-reflection heterodyne interferometer. *Appl. Opt.* **2014**, *53*, 1903–1908. [CrossRef]
22. Ma, T.; Wang, W.-H. Sub-Arc Accuracy Small Angle Measurement Based on Dual Mirrors Reflections. *Flight Control Detect.* **2019**, *2*, 84–89.
23. Mao, S.; Wang, Z.; Pan, J. Microscope 3D Point Spread Function Evaluation Method on a Confirmed Object Plane Perpendicular to the Optical Axis. *Appl. Sci.* **2020**, *10*, 2430. [CrossRef]
24. Zhou, S.; Zhang, Z.-W.; Cai, R.-B. High Precision Micro Displacement Measurement System Based on PSD. *Flight Control Detect.* **2020**, *18*, 22–27.
25. Yang, Y.-P. Development and application of position sensitive detector. *Sci-Tech Inf. Dev. Econ.* **2006**, *24*, 183–185.
26. Faisal, A.R.M.; Nguyen, T.; Dinh, T.; Nguyen, T.K.; Tanner, P.; Streed, E.W.; Dao, D.V. 3C-SiC/Si hetero structure: An excellent platform for position-sensitive detectors based on photovoltaic effect. *ACS Appl. Mater. Interfaces* **2019**, *11*, 55–58. [CrossRef] [PubMed]
27. He, Y.; Mi, F.; Jin, W.; Liu, M.; Hu, L. Design of an autocollimator swing micro-mirror angle measurement system based on PSD. *Opt. Tech.* **2017**, *43*, 561–565.

Disclaimer/Publisher's Note: The statements, opinions and data contained in all publications are solely those of the individual author(s) and contributor(s) and not of MDPI and/or the editor(s). MDPI and/or the editor(s) disclaim responsibility for any injury to people or property resulting from any ideas, methods, instructions or products referred to in the content.